PAPER • OPEN ACCESS

Bionic microchannels for step lifting transpiration

View the article online for updates and enhancements.

Bionic microchannels for step lifting transpiration

Zhaolong Wang[1,*] , **Qiu Yin**[2], **Ziheng Zhan**[1], **Wenhao Li**[1], **Mingzhu Xie**[1], **Huigao Duan**[1] , **Ping Cheng**[2], **Ce Zhang**[3], **Yongping Chen**[4,5,*] **and Zhichao Dong**[6,*]

[1] Interdisciplinary Research Center of Low-carbon Technology and Equipment, College of Mechanical and Vehicle Engineering, Hunan University, Changsha 410082, People's Republic of China
[2] MOE Key Laboratory for Power Machinery and Engineering, School of Mechanical Engineering, Shanghai Jiao Tong University, Shanghai 200240, People's Republic of China
[3] Qian Xuesen Laboratory of Space Technology, China Academy of Space Technology (CAST), Beijing 100094, People's Republic of China
[4] Jiangsu Key Laboratory of Micro and Nano Heat Fluid Flow Technology and Energy Application, School of Environmental Science and Engineering, Suzhou University of Science and Technology, Suzhou, Jiangsu 215009, People's Republic of China
[5] Key Laboratory of Energy Thermal Conversion and Control of Ministry of Education, School of Energy and Environment, Southeast University, Nanjing 210096, People's Republic of China
[6] Chinese Academy of Sciences Key Laboratory of Bio-inspired Materials and Interface Sciences, Technical Institute of Physics and Chemistry, Chinese Academy of Sciences, 100190 Beijing, People's Republic of China

E-mail: zhaolongwang@hnu.edu.cn, ypchen@seu.edu.cn and dongzhichao@mail.ipc.ac.cn

Abstract

Those various cross-sectional vessels in trees transfer water to as high as 100 meters, but the traditional fabrication methods limit the manufacturing of those vessels, resulting in the non-availability of those bionic microchannels. Herein, we fabricate those bionic microchannels with various cross-sections by employing projection micro-stereolithography (PμSL) based 3D printing technique. The circumradius of bionic microchannels (pentagonal, square, triangle, and five-pointed star) can be as small as 100 μm with precisely fabricated sharp corners. What's more, those bionic microchannels demonstrate marvelous microfluidic performance with strong precursor effects enabled by their sharp corners. Most significantly, those special properties of our bionic microchannels enable them outstanding step lifting performance to transport water to tens of millimeters, though the water can only be transported to at most 20 mm for a single bionic microchannel. The mimicked transpiration based on the step lifting of water from bionic microchannels is also achieved. Those precisely fabricated, low-cost, various cross-sectional bionic microchannels promise applications as microfluidic chips, long-distance unpowered water transportation, step lifting, mimicked transpiration, and so on.

Supplementary material for this article is available online

Keywords: bionic microchannel, microfluidics, water transportation, step lifting, 3D printing

---

* Authors to whom any correspondence should be addressed.

1. Introduction

According to the cohesion-tension theory proposed by Dixon and Joly in 1894 [1], the water loss caused by transpiration reduces the pressure of the water in leaves lower than atmospheric pressure [2–4]. The reduced pressure from transpiration and the capillary force from microscale vessels rise the water from soil to the leaves to maintain hydration [5]. Directional antigravity water transportation via xylem is the key factor for natural trees to grow higher, even though water gravity and path length resistance drastically increase with the height of trees [6]. Far more than an interesting natural phenomenon, researchers have done lots of work focusing on such a phenomenon in the past few decades due to their potential applications such as oil recovery [7], solar steam generator [8–10], water diode [11], and so on [12, 13]. However, the limitation of those vessels with various cross-sections and sharp corners challenges us a lot, and the unrealized fabrication of those bionic microchannels severely limits their experimental study and practical applications.

Numerous efforts have gone into the fabrication of microchannels by employing various planar approaches [14]. Soft lithography technique can be used to produce arrayed microchannels. In addition, micro-hot embossing and etching techniques have been employed for fabrication of those microchannels with high aspect ratio of height and width. Meanwhile, people make use of micro-injection molding to process some integrated microfluidic system [15, 16]. However, those previously used methods cost a lot of time and money for fabricating even simple microchannels. On the other hand, those methods are limited to manufacture 2D structures, and it is difficult to fabricate various cross-sectional microchannels simple and cheap at hand [17]. With the development of microchannels in recent years, more and more researchers find that 3D microchannels with non-circular and non-rectangular cross-sections demonstrate better microfluidic performance [18, 19]. Most importantly, it has been shown that bionic science makes a significant difference on designing next generation unpowered water transportation devices [20, 21]. Therefore, fabrication of bionic microchannels with various cross-sections is in urgent need for those various significant potential applications.

The fast development of 3D printing technique brings the dawn for solving such an issue [22–25]. As a layer by layer manufacturing method, 3D printing technique can not only fabricate arbitrary shaped complex structures, but also satisfy the requirements of 'what you see becomes what you get as soon as possible' [26, 27]. Based on 3D printing technologies, numerous achievements about tissue engineering [28, 29], MEMS [22], metamaterial [30, 31], battery [32, 33], microrobots [34, 35], wearable devices [36, 37], human-machine interface, etc [38, 39] have been obtained. Recently, the 3D printed bioinspired surfaces and channels are attracting more and more attention [40–43]. Among which, unique structures from araucaria leaf [2], nepenthes alata [21], mosquito eyes [44], springtail [45], cicada wings [46], lacewing [47], water strider [48], and hummingbird tongue [13] have been mimicked. Recently, cellular fluidics [49] has also been proposed inspired by porous microchannels inside trees. However, the bionic microchannels with various cross-sections are merely fabricated and experimentally studied. Herein, inspired by the vessels in trees, we proposed an innovative way to fabricate various cross-sectional bionic microchannels by using the projection micro-stereolithography (PμSL) based 3D printing technique, which could precisely tailor the geometric features of the structures based on the accumulation of material inside photo-curable resin. The precisely printed bionic microchannels demonstrate marvelous microfluidic performance by elevating water with an ultrahigh speed. Most significantly, the various cross-sectional bionic microchannels are also used for the mimicked transpiration with their extraordinary performance on antigravity step lifting of water.

2. Results and discussion

2.1. Fabrication and characterization of bionic microchannels

Capillary force inside the vessels in trees enables the antigravity water transportation within it (figure 1(ai)), which provides sufficient water for the leaves through arbitrary cross-sectional microchannels (figures 1(aii) and (aiii). Herein, inspired by the vessels inside trees, we designed and fabricated microchannels with various cross-sections by using PμSL based 3D printing technique with hydrophilic photo-curable resin (figures 1(b) and S1, supporting information). The contact angle of a printed flat surface is around 55° (figure S2, supporting information). As shown in figure 1(c), circular microchannel, pentagonal microchannel, square microchannel, triangle microchannel, as well as five-pointed star microchannel are designed based on those various cross-sectional vessels inside trees. Furthermore, micro-computerized tomography (micro-CT) images demonstrate the detailed inner morphologies of the printed bionic microchannels (figures 1(d) and S3, S4, supporting information), demonstrating that the inside morphologies of those printed various cross-sectional microchannels are well consistent with the designed geometric parameters.

We vertically inserted those printed bionic microchannels with different sizes and morphologies into a reservoir full of dyed water to study their microfluidic and self-siphon performance (figure S5, movie S1, supporting information). The blue dyed water is employed to enhance the visualization. We find that all of these various cross-sectional bionic microchannels present marvelous self-siphon behavior (figures 1(e), (f) and S5, supporting information). However, the flowing speed of the water inside different cross-sectional microchannels varies a lot. Specifically, a five-pointed star microchannel presents the fastest flowing speed among all of those various cross-sectional bionic microchannels, while a circular microchannel shows the slowest microfluidic velocity (figure 1(e)). Moreover, the final states of water inside these bionic microchannels also vary a lot due to the morphologies of them (figure S6, supporting information). The water is well bound inside a five-pointed star microchannel. However, the water flowing in pentagon microchannels is not confined well, and the water came out a little at the end of the microchannel (figure 1(f)).
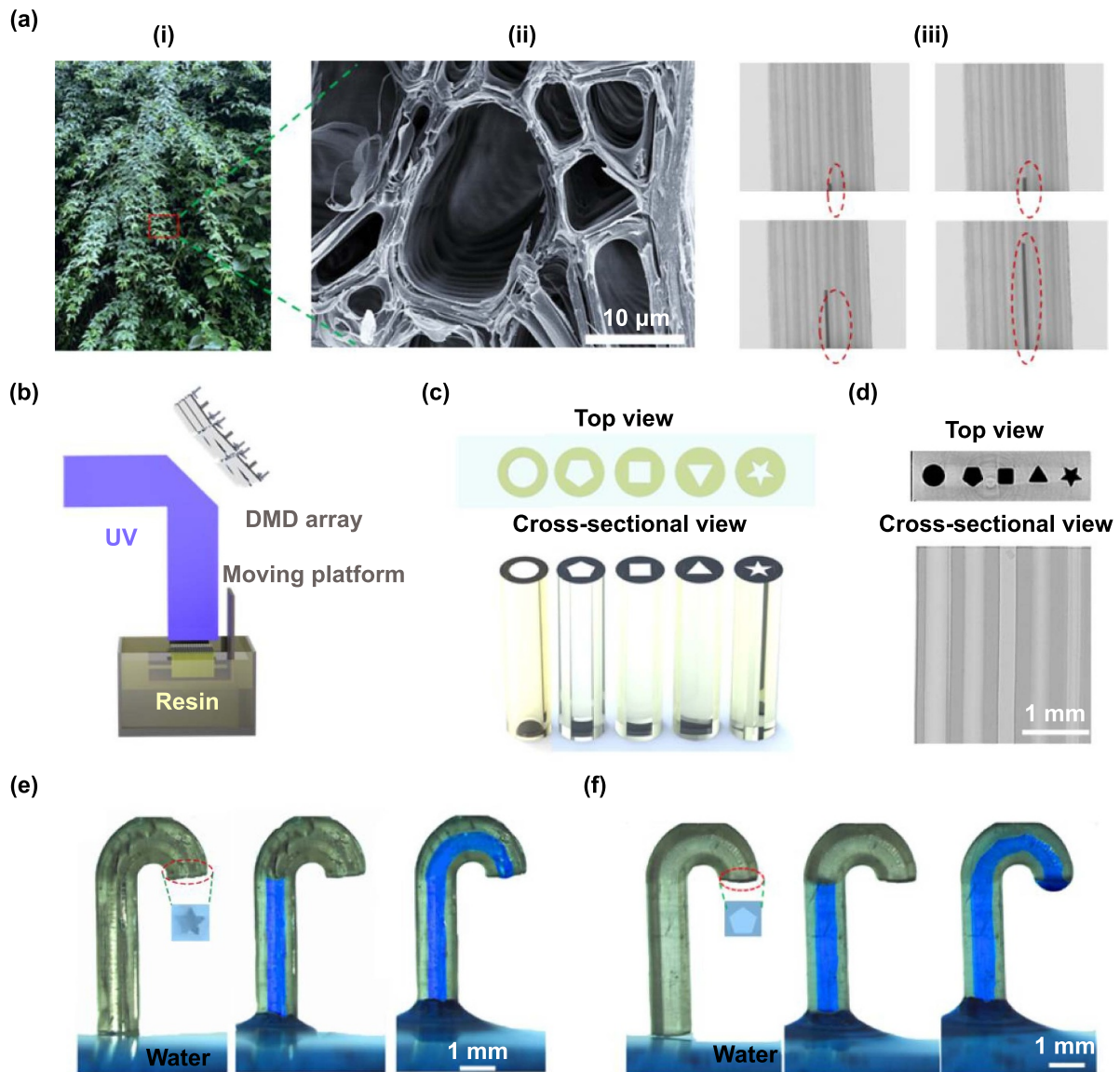
Figure 1. Design and fabrication of various cross-sectional bionic microchannels by PμSL based 3D printing technique. (a) Vessels with arbitrary cross-sections inside a tree. (b) Schematic of the fast up-bottom fabrication by a PμSL based 3D printing technique. (c) Cross-sectional schematic view of the 3D printed mimicked microchannels. (d) Top and cross-sectional views of the morphologies of fabricated microchannels obtained from micro-CT. (e) and (f) Self-siphon phenomenon inside two different cross-sectional bionic microchannels.

2.2. Microfluidic performance of bionic microchannels

The capillary force is mainly affected by the cross-section and size of microchannels, liquid-air surface tension, as well as the contact angle of materials for microchannels [50]. We studied the influence of the bionic microchannel's cross-sections on the capillary fluidic performance for those bionic microchannels by setting their circumcircle's diameter and length to 400 μm and 20 mm, respectively. In addition, the internal angle of five-pointed star microchannels is 36° (figures 2(a) and (b)). The cross-sections of the microchannels make a big difference on the water transportation speed obviously. We find that the velocity of the water increases with the decrease of the corner's angle (movie S2, supporting information). The slowest average velocity of a circular microchannel is

31 mm s^{-1}, while a five-pointed star microchannel presents a higher microfluidic velocity, which is 46 mm s^{-1} (figure 2(a)). Moreover, the microfluidic performance of different cross-sectional microchannels is shown in figure 2(b). The results reveal that the difference mainly originates from the different velocity at the end of the microchannels due to the different capillary forces based on their cross-sections.

We further studied the effects of corner's angle inside of the microchannels on their microfluidic performance by varying the internal angle (ψ) of 20 mm length five-pointed star microchannels (figure 2(c)). The average velocity of the water inside the bionic five-pointed star microchannels reaches the maximum about 46 mm s^{-1} when the internal angle (ψ) is 36°, while the average velocity decreases with the increase of ψ (movie S3, supporting information). Figures 2(d) and
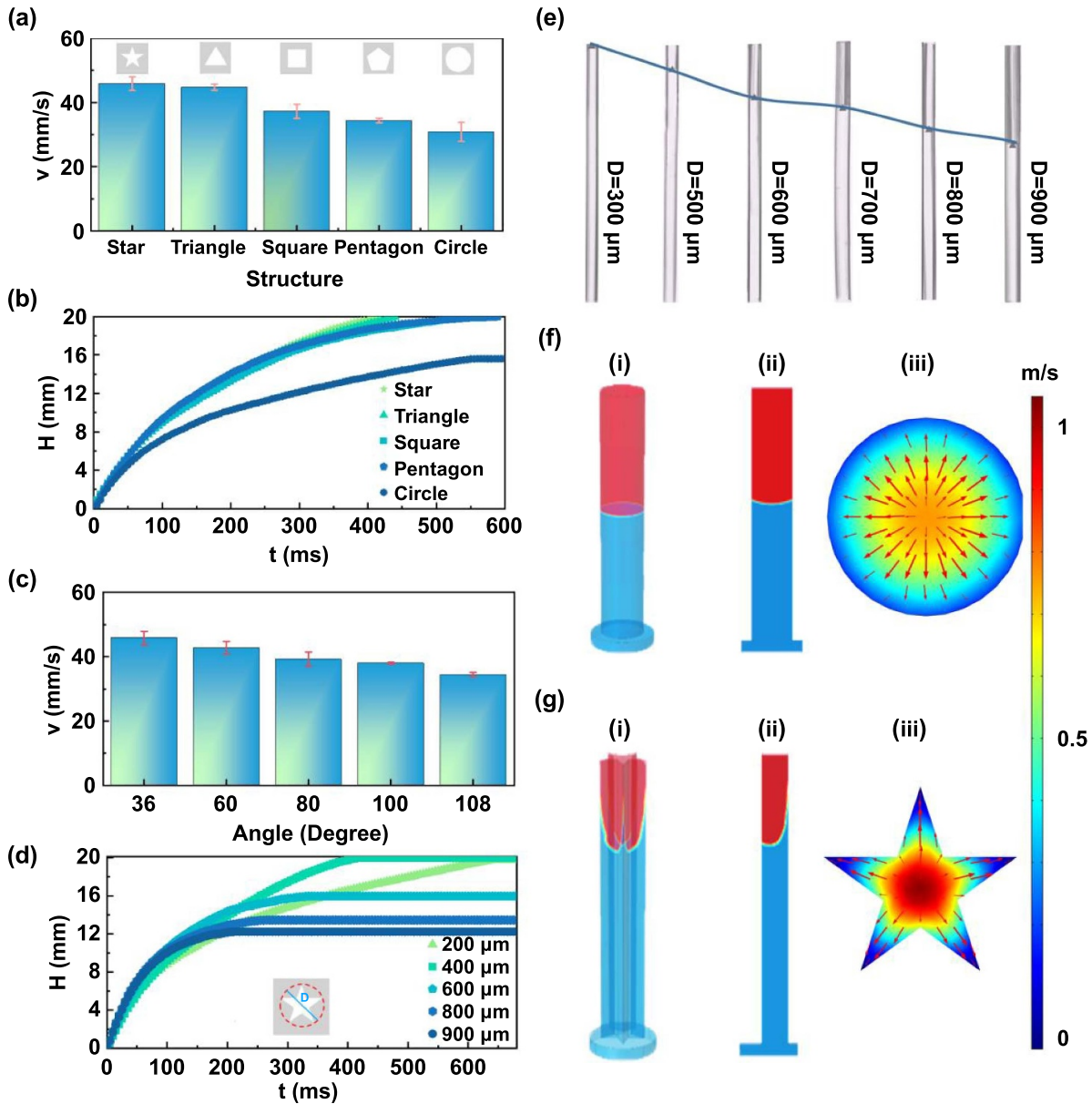
Figure 2. Microfluidic performance of various cross-sectional microchannels. (a) The average water transportation velocity for different cross-sectional microchannels. (b) The microfluidic performance of different cross-sectional microchannels. (c) The influence of internal angle (ψ) of five-pointed star microchannels on water transportation velocity. (d) The microfluidic performance of five-pointed star microchannels with different sizes (*D*). (e) The influence of *D* on water transportation velocity for five-pointed star microchannels. (f) and (g) The calculated microfluidic performance of circular and five-pointed star microchannels.

(e) present the effects of microchannel's size on its microfluidic performance by using five-pointed star microchannels with $\psi = 36°$. The average velocity of the water transportation inside microchannels increases with the increase of the circumcircle diameter before reaching the maximum with a circumcircle diameter of 400 μm (movie S4, supporting information). The combination effects of weak entrance effect and fast transportation velocity after entering the microchannels contribute to the fastest average velocity for one with a circumcircle diameter of 400 μm. Then, the average velocity decreases with the increase of the circumcircle diameter afterwards. In addition, all of these microchannels with a circumcircle diameter smaller than 400 μm are filled with water.

However, when the circumcircle diameter of five-pointed star microchannels is larger than 400 μm, the water is unable to arrive at the top of the microchannels with a height of 20 mm (figure 2(e)). Also, the larger the circumcircle diameter of the microchannel, the lower the height the water can reach.

The comparison of the microfluidic performance for a circular and a five-pointed star microchannel has also been revealed by the calculation (figures 2(f) and (g)). The cross-sections of bionic microchannels make a big difference on the meniscus phenomenon within the microchannels. A five-pointed star microchannel demonstrates larger meniscus angle comparing with that of a circular one. In addition, a five-star microchannel exhibits strong precursor phenomenon which
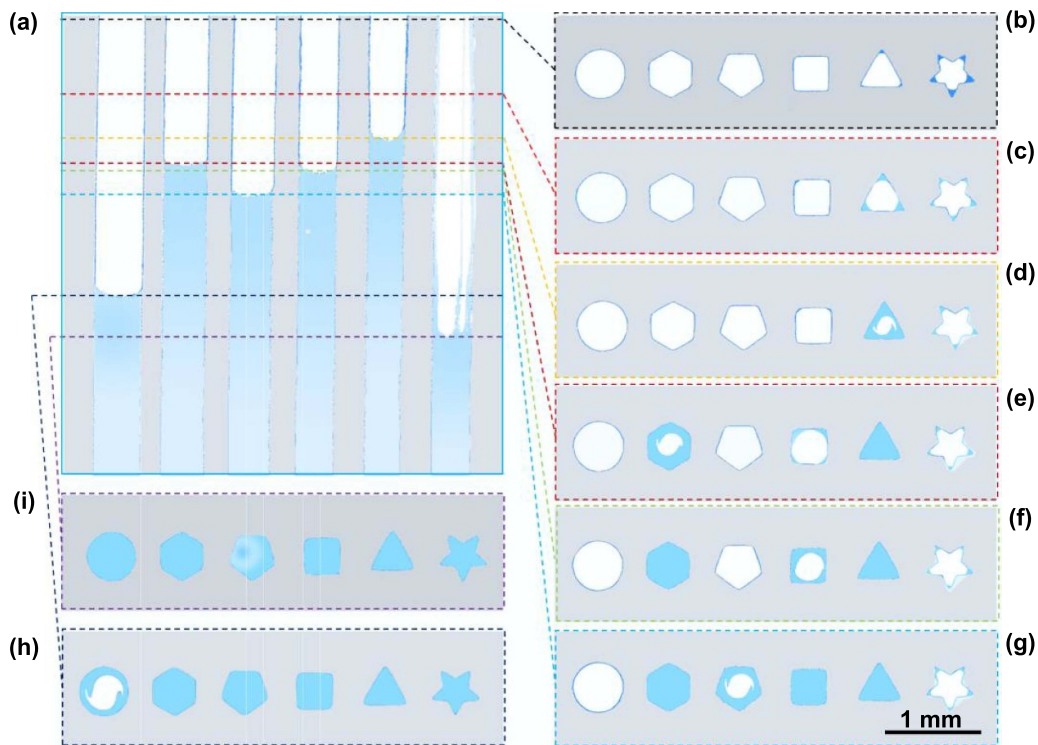
Figure 3. 3D wetting states of microchannels obtained from Micro-CT. (a) Front view of the 3D wetting state of water capillary rise inside of different cross-sectional microchannels. (b)–(i) Top view of the 3D wetting state of water capillary rise inside different bioinspired microchannels from the top to the bottom.

cannot be found inside a circular microchannel. As a result, the capillary force for antigravity and acceleration of water along the axial direction of a five-pointed star microchannel is much larger than that inside a circular one (figures 2(fiii) and (giii)). The flowing characteristics of those other cross-sectional microchannels are also calculated (figure S7, supporting information).

Micro-CT was also used to reveal the different microfluidic performance of various cross-sectional bionic microchannels (figure 3). The water reaches different heights within different cross-sectional microchannels with a five-pointed star microchannel presents the best microfluidic performance at the same time (figure 3(a)), which is consistent with the results in figure 2. The five-pointed star microchannel exhibits the best water precursor effect (figure 3(b)), resulting in the fastest water transportation (figure 2(a)). In addition, triangular and rectangular microchannels also exhibits strong precursor effect (figures 3(c) and (d)), which contributes a lot to their amazing microfluidic performance. In contrast, there is almost no precursor effect for those other kinds of bionic microchannels because there are no sharp corners inside of them (figure 3(ei)). In addition, it can be seen that the velocity of precursor is almost triple of that of the bulk water inside a five-pointed star microchannel (figure 3(b)). The results clearly reveal that there is stronger precursor effect for a bionic microchannel with sharper corners. The higher water flowing velocity inside such a microchannel (figure 2(d)) demonstrate that the precursor effect dominates the marvelous microfluidic performance of various cross-sectional bionic microchannels, especially for five-pointed star microchannels.

2.3. Mimicked step lifting transpiration

The capillary force for the antigravity water transportation ($h = 2\gamma\cos\theta / \rho g r$ with $\gamma, \theta, \rho, g, r$ are respectively liquid-air surface tension, contact angle, density of liquid, local acceleration due to gravity, and the radius of channel) within a single bionic microchannel is limited. We experimentally studied the step lifting phenomenon by using our bionic microchannels whose length was 20 mm each with a diameter of 400 μm (figure 4(a)). Water is transported from the reservoir to the top end of the first layered microchannels due to the capillary force. Then, the water come out from the end of microchannels with absorbent paper on the first stage. Next, the second layered microchannels absorb the water from the absorbent paper on the first stage and transport the water to the second stage. Repeatedly, the water will be step lifted to higher and higher stages. The results show that the dyed water can be elevated to more than 60 mm, even though the length of a single microchannel is only 20 mm, demonstrating that the infinite anti-gravity water transportation can be achieved by our bionic microchannels with step lifting stage by stage.

Based on step lifting phenomenon enabled by our bionic microchannels, we carried out a series of experiments to imitate transpiration of plants to absorb water from a tank, transport it via step lifting with the bionic microchannels and release water to air enabled by photothermal effect of laser (figure 4(b)). The wavelength of our laser is 795 nm. We employ regularly arranged various cross-sectional bionic microchannels to step lift water for transpiration. The length of a single five-pointed star microchannel is 20 mm with a
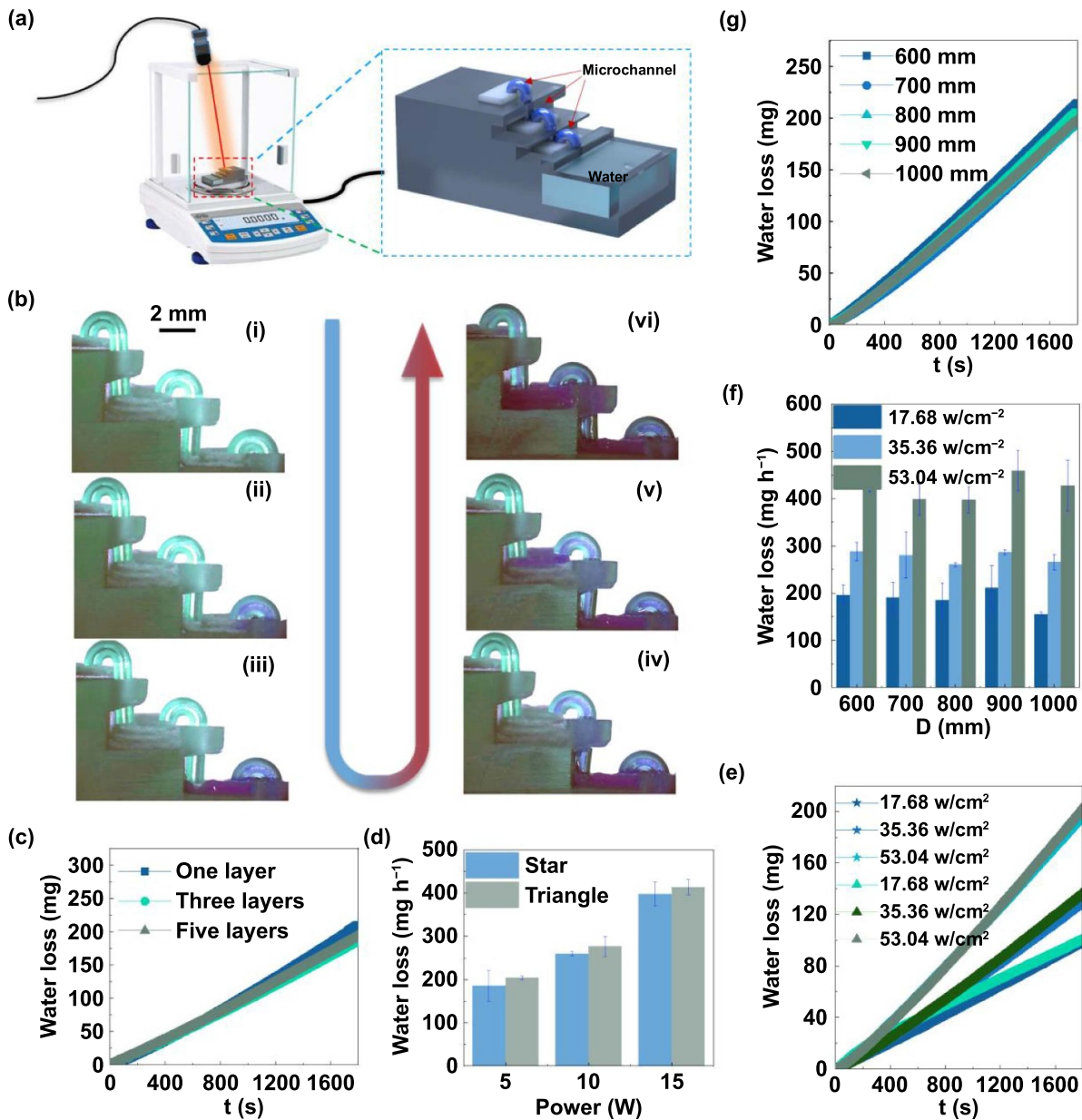
Figure 4. Step lifting for mimic transpiration. (a) Water step lifting. (b) Experimental setup for testing the performance of mimicked transpiration. (c) The relationship between the layers of step lifting and water loss. (d) The effects of microchannel's cross-sections on water loss at different light intensities. (e) Real-time tests of water loss for triangle and five-pointed star microchannels. (f) The relationship between the size of bionic microchannels and mass loss. (g) Real-time tests of water loss for different sized bionic microchannels.

circumcircle diameter of 400 μm. It can be seen that the number of stages almost makes no difference on the water evaporation rate by our step lifting structure (figure 4(c)), validating its great performance on step lifting mimicked transpiration. Then, we chose a three layered step lifting structure for further investigation of mimicked transpiration. The water mass loss rate shows almost no dependence on the cross-sections of bionic microchannels, but the intensity of the laser affects the water evaporation rate a lot (figures 4(d) and (e)). The reason is that the water transportation capability of different cross-sectional microchannels enabled by the capillary force is much higher than the water evaporation rate. As a result, the

water evaporation rate increases with the increase of the laser intensity.

We chose five-pointed star microchannels to study the effects of sizes on their imitated transpiration performance. Similarly, the sizes of the bionic microchannels make little difference on the water evaporation rate because the laser intensity dominates such a process, which can be validated by the increasing water evaporation rate with the increase of the laser intensity (figures 4(f) and (g)). We also fabricated an artificial tree trunk (figure S8, supporting information) with regularly arranged various cross-sectional bionic microchannels. As shown in figure S8(a), supporting information, the

geometry parameters of different cross-sectional microchannels are precisely controlled, and the distance between two adjacent bionic microchannels can also be adjusted accurately. Similar to the mimicked transpiration for a single bionic microchannel, the water evaporation rate for such a mimicked 'tree trunk' is mainly affected by the laser intensity (figure S8b, supporting information), though the total evaporation rate is tens of times of that with only one single bionic microchannel irradiated by the same laser intensity.

3. Conclusion

A series of various cross-sectional bionic microchannels inspired by vessels inside trees with marvelous microfluidic performance were designed and fabricated by using PμSL based 3D printing technique. The microfluidic performance of bionic microchannels depends on their sizes and cross-sections, and a five-pointed star microchannel presents the best microfluidic performance among all of those various cross-sectional bionic microchannels. Inspired by the infinite water antigravity transportation of natural trees, we additionally fabricated a stepped structure with parallel bionic microchannels, which exhibits marvelous step lifting performance because of the remarkable antigravity water transportation performance of our bionic microchannels. Most significantly, mimicked transpiration was carried out based on the merits of our various cross-sectional bionic microchannels and their step lifting performance irradiated by a laser, achieving a maximum vaporization rate of 500 mg h^{-1} for a single microchannel. We believe that our various cross-sectional bionic microchannels enable better design of microfluidic devices, which promise them wide applications for solar water evaporation, biodetection, microfluidic chips, heat sink, and so on.

4. Materials and methods

4.1. Fabrication of various cross-sectional microchannels

The proposed various cross-sectional bionic microchannels were fabricated by PμSL based 3D printing technique (BMF-P140, China), who demonstrates fast manufacturing speed and high precision in a layer-by-layer manner with the most advanced digital micro-display (DMD) technology. We firstly designed and built 3D models by a CAD software, and then those 3D structures were sliced into a lot of 2D digital images with corresponding cross-sectional structures. After that, these images were transferred to the DMD as the dynamic mask patterns. For different structures, we control the exposure time (405 nm UV light) to the liquid resin. Then, a layer is solidified on the platform with the similar feature of the first 2D pattern. Next, the platform moves down below the photo-curable resin, and the resin flows smoothly after staying for a few seconds. Finally, a new layer is fabricated on the top of the former layer with the same way. Such a process is repeated until the whole structure is fabricated. The biggest projection area is 14.5 mm × 8.2 mm with a resolution of 1920 × 1080, and a pixel size is 7.56 μm × 7.56 μm.

4.2. Measurement of water transportation inside of bionic microchannels

We tested the water transportation process inside of our bionic microchannels with a high-speed camera (NAC Memrecam HX-7 s). First, we filled a large petri dish with dyed water as a reservoir. Then, we inserted our printed bionic microchannels into the reservoir vertically and slowly. The whole process was recorded by the high-speed camera.

4.3. Mimicked transpiration

First, water was sucked from the reservoir to the top of the artificial leaf (fiber). Then, the laser irradiated on the evaporator for water evaporation. The weight of the water in reservoir was monitored by an electronic microbalance with an accuracy of 0.001 g in real-time (Radwag AS 60.220.R2).

4.4. Characterization of morphology

The cross-sectional shapes of these bionic microchannels were characterized by a microscope (MJ31, Mshot) first. Then, the detailed inner morphologies of these bionic microchannels were measured by a micro-CT (Skyscan 1272).

4.5. Measurement of the contact angle

The contact angle was tested by a measuring device from SINDIN Company (SDC-100). We placed a printed flat surface on the stage of the measuring device. Then, a 2 μl water droplet squeezed out from a syringe needle was placed on the top of the printed flat surface. Finally, the side view of the droplet placed on the printed flat surface was transmitted by an acquisition system to a software to obtain the contact angle.

4.6. Simulation of the microfluidic performance inside of bionic microchannels

The simulation is conducted based on the two-phase level-set method with a commercial software (COMSOL Multiphysics 5.3) by considering all of the inertial effects, dynamic effects, and incident effects.

Conflict of interest

The authors declare no conflict of interest.

ORCID iDs

Zhaolong Wang　https://orcid.org/0000-0003-2967-4546
Huigao Duan　https://orcid.org/0000-0001-9144-2864

References

[1] Dixon H H and Joly J 1895 XII. On the ascent of sap *Phil. Trans. R. Soc.* B **186** 563–76

[2] Xu J K, Xiu S Y, Lian Z X, Yu H D and Cao J J 2022 Bioinspired materials for droplet manipulation: principles, methods and applications *Droplet* **1** 11–37

[3] Feng S L, Zhu P G, Zheng H X, Zhan H Y, Chen C, Li J Q, Wang L Q, Yao X, Liu Y H and Wang Z K 2021 Three-dimensional capillary ratchet-induced liquid directional steering *Science* **373** 1344–8

[4] Yong J L, Yang Q, Huo J L, Hou X and Chen F 2022 Underwater gas self-transportation along femtosecond laser-written open superhydrophobic surface microchannels (<100 μm) for bubble/gas manipulation *Int. J. Extrem. Manuf.* **4** 015002

[5] Wheeler T D and Stroock A D 2008 The transpiration of water at negative pressures in a synthetic tree *Nature* **455** 208–12

[6] Koch G W, Sillett S C, Jennings G M and Davis S D 2004 The limits to tree height *Nature* **428** 851–4

[7] Beebe D J, Mensing G A and Walker G M 2002 Physics and applications of microfluidics in biology *Annu. Rev. Biomed. Eng.* **4** 261–86

[8] Sackmann E K, Fulton A L and Beebe D J 2014 The present and future role of microfluidics in biomedical research *Nature* **507** 181–9

[9] Stoock A D, Dertinger S K W, Ajdari A, Mezić I, Stone H A and Whitesides G M 2002 Chaotic mixer for microchannels *Science* **295** 647–51

[10] Wang Z L, Zhan Z H, Chen L, Duan G H, Cheng P, Kong H, Chen Y P and Duan H G 2022 3D-printed bionic solar evaporator *Sol. RRL* **6** 2101063

[11] Yager P, Edwards T, Fu E, Helton K, Nelson K, Tam M R and Weigl B H 2006 Microfluidic diagnostic technologies for global public health *Nature* **442** 412–8

[12] Chen L, Duan G H, Zhang C, Cheng P and Wang Z L 2022 3D printed hydrogel for soft thermo-responsive smart window *Int. J. Extrem. Manuf.* **4** 025302

[13] Wang Z L, Li Y Y, Gong S, Li W H, Duan H G, Cheng P, Chen Y P and Dong Z C 2022 Three-dimensional open water microchannel transpiration mimetics *ACS Appl. Mater. Interfaces* **14** 30435–42

[14] Fan D L *et al* 2022 Self-shrinking soft demoulding for complex high-aspect-ratio microchannels *Nat. Commun.* **13** 5083

[15] Zheng B, Tice J D and Ismagilov R F 2004 Formation of arrayed droplets by soft lithography and two-phase fluid flow, and application in protein crystallization *Adv. Mater.* **16** 1365–8

[16] Mair D A, Geiger E, Pisano A P, Fréchet J M and Svec F 2006 Injection molded microfluidic chips featuring integrated interconnects *Lab Chip* **6** 1346–54

[17] Yuan R, Lee J, Su H W, Levy E, Khudiyev T, Voldman J and Fink Y 2018 Microfluidics in structured multimaterial fibers *Proc. Natl Acad. Sci. USA* **115** e10830–8

[18] Parekh D P, Ladd C, Panich L, Moussa K and Dickey M D 2016 3D printing of liquid metals as fugitive inks for fabrication of 3D microfluidic channels *Lab Chip* **16** 1812–20

[19] Kim S M and Mudawar I 2010 Analytical heat diffusion models for different micro-channel heat sink cross-sectional geometries *Int. J. Heat Mass Transfer* **53** 4002–16

[20] Chen H W, Zhang P F, Zhang L W, Liu H L, Jiang Y, Zhang D Y, Han Z W and Jiang L 2016 Continuous directional water transport on the peristome surface of nepenthes alata *Nature* **532** 85–89

[21] Li C X, Dai H Y, Gao C, Wang T, Dong Z C and Jiang L 2019 Bioinspired inner microstructured tube controlled capillary rise *Proc. Natl Acad. Sci. USA* **116** 12704–9

[22] Ge Q, Li Z Q, Wang Z L, Kowsari K, Zhang W, He X N, Zhou J L and Fang N X 2020 Projection micro stereolithography based 3D printing and its applications *Int. J. Extrem. Manuf.* **2** 022004

[23] Zhu J Z, Zhang Q, Yang T Q, Liu Y and Liu R 2020 3D printing of multi-scalable structures via high penetration near-infrared photopolymerization *Nat. Commun.* **11** 3462

[24] Scott S M, Mueller J, Visser C W and Lewis A J 2019 Voxelated soft matter via multimaterial multinozzle 3D printing *Nature* **575** 330–5

[25] Huang Y A *et al* 2021 Programmable robotized 'transfer-and-jet' printing for large, 3D curved electronics on complex surfaces *Int. J. Extrem. Manuf.* **3** 045101

[26] He Y, Xiao X, Wu Y and Fu J Z 2015 A facile and low-cost micro fabrication material: flash foam *Sci. Rep.* **5** 13522

[27] Zhang W Q, Ye H T, Feng X B, Zhou W Z, Cao K, Li M Y, Fan S F and Lu Y 2022 Tailoring mechanical properties of PμSL 3D-printed structures via size effect *Int. J. Extrem. Manuf.* **4** 045201

[28] Bose S, Vahabzadeh S and Bandyopadhyay A 2013 Bone tissue engineering using 3D printing *Mater. Today* **16** 496–504

[29] Xing J F, Zheng M L and Duan X M 2015 Two-photon polymerization microfabrication of hydrogels: an advanced 3D printing technology for tissue engineering and drug delivery *Chem. Soc. Rev.* **44** 5031–9

[30] Wang Z L, Yang P Y, Qi G G, Zhang Z M and Cheng P 2020 An experimental study of a nearly perfect absorber made from a natural hyperbolic material for harvesting solar energy *J. Appl. Phys.* **127** 233102

[31] Wang Z L, Liu Z, Duan G H, Fang L Y and Duan H G 2022 Ultrahigh broadband absorption in metamaterials with electric and magnetic polaritons enabled by multiple materials *Int. J. Heat Mass Transfer* **185** 122355

[32] Zhao J K, Wei D N, Wang J J, Yang K M, Wang Z L, Chen Z J, Zhang S G, Zhang C and Yang X J 2022 Inorganic crosslinked supramolecular binder with fast self-healing for high performance silicon based anodes in lithium-ion batteries *J. Colloid Interface Sci.* **625** 373–82

[33] Zhao J K, Bao K, Xie M Z, Wei D N, Yang K M, Zhang X B, Zhang C, Wang Z L and Yang X J 2022 Two-dimensional ultrathin networked CoP derived from Co(OH)$_2$ as efficient electrocatalyst for hydrogen evolution *Adv. Compos. Hybrid Mater.* **5** 2421–8

[34] Zhan Z H, Chen L, Duan H G, Chen Y Q, He M and Wang Z L 2022 3D printed ultra-fast photothermal responsive shape memory hydrogel for microrobots *Int. J. Extrem. Manuf.* **4** 015302

[35] Li B S *et al* 2022 Viral infection and transmission in a large, well-traced outbreak caused by the SARS-CoV-2 delta variant *Nat. Commun.* **13** 460

[36] Chen L, Wang Z L, Zhan Z H, Xie M Z, Duan G H, Cheng P, Chen Y Q and Duan H G 2021 3D printed super-anti-freezing self-adhesive human-machine interface *Mater. Today Phys.* **19** 100404

[37] Wang Z L, Li W H, Chen L, Zhan Z H and Duan H G 2022 3D printable silicone rubber for long-lasting and weather-resistant wearable devices *ACS Appl. Polym. Mater.* **4** 2384–92

[38] Wei T S, Ahn B Y, Grotto J and Lewis J A 2018 3D printing of customized Li-ion batteries with thick electrodes *Adv. Mater.* **30** 1703027

[39] Schaffner M, Faber J A, Pianegonda L, Rühs P A, Coulter F and Studart A R 2018 3D printing of robotic soft actuators

with programmable bioinspired architectures *Nat. Commun.* **9** 878

[40] Yin Q, Guo Q, Wang Z L, Chen Y Q, Duan H G and Cheng P 2021 3D-printed bioinspired cassie–baxter wettability for controllable microdroplet manipulation *ACS Appl. Mater. Interfaces* **13** 1979–87

[41] Chen H W, Ran T, Gan Y, Zhou J J, Zhang Y, Zhang L W, Zhang D Y and Jiang L 2018 Ultrafast water harvesting and transport in hierarchical microchannels *Nat. Mater.* **17** 935–42

[42] Liu X J, Gu H C, Wang M, Du X, Gao B B, Elbaz A, Sun L D, Liao J L, Xiao P F and Gu Z Z 2018 3D printing of bioinspired liquid superrepellent structures *Adv. Mater.* **30** 1800103

[43] Xie M Z, Duan H G, Cheng P, Chen Y P, Dong Z C and Wang Z L 2022 Underwater unidirectional cellular fluidics *ACS Appl. Mater. Interfaces* **14** 9891–8

[44] Wang L, Wang R X, Wang J and Wong T S 2020 Compact nanoscale textures reduce contact time of bouncing droplets *Sci. Adv.* **6** eabb2307

[45] Gundersen H, Leinaas H P and Thaulow C 2014 Surface structure and wetting characteristics of Collembola cuticles *PLoS One* **9** e86783

[46] Oh J, Dana C E, Hong S, Román J K, Jo K D, Hong J W, Nguyen J, Cropek D M, Alleyne M and Miljkovic N 2017 Exploring the role of habitat on the wettability of cicada wings *ACS Appl. Mater. Interfaces* **9** 27173–84

[47] Hu H M, Watson J A, Cribb B W and Watson G S 2011 Fouling of nanostructured insect cuticle: adhesion of natural and artificial contaminants *Biofouling* **27** 1125–37

[48] Wagner T, Neinhuis C and Barthlott W 1996 Wettability and contaminability of insect wings as a function of their surface sculptures *Acta Zool* **77** 213–25

[49] Dudukovic N A, Fong E J, Gemeda H B, DeOtte J R, Cerón M R, Moran B D, Davis J T, Baker S E and Duoss E B 2021 Cellular fluidics *Nature* **595** 58–65

[50] Jong W R, Kuo T H, Ho S W, Chiu H H and Peng S H 2007 Flows in rectangular microchannels driven by capillary force and gravity *Int. Commun. Heat Mass Transfer* **34** 186–96